Available online at www.sciencedirect.com
ScienceDirect
Journal of Power Sources 179 (2008) 155–163
JOURNAL OF POWER SOURCES
www.elsevier.com/locate/jpowsour

Applications of one-cycle control to improve the interconnection of a solid oxide fuel cell and electric power system with a dynamic load

Allie E. Auld [a,b], Fabian Mueller [a], Keyue Ma Smedley [b], Scott Samuelsen [a], Jack Brouwer [a,*]

[a] National Fuel Cell Research Center, University of California, Irvine, CA 92697-3550, United States
[b] Power Electronics Laboratory, Department of Electrical Engineering and Computer Science, University of California, Irvine, CA 92697, United States

Received 9 November 2007; received in revised form 18 December 2007; accepted 19 December 2007
Available online 28 December 2007

Abstract

Adding distributed generation (DG) is a desirable strategy for providing highly efficient and environmentally benign services for electric power, heating, and cooling. The interface between a solid oxide fuel cell (SOFC), typical loads, and the electrical grid is simulated in Matlab/Simulink and analyzed to assess the interactions between DG and the electrical grid. A commercial building load profile is measured during both steady-state and transient conditions. The load data are combined with the following models that are designed to account for physical features: a One-Cycle Control grid-connected inverter, a One-Cycle Control active power filter, an SOFC, and capacitor storage. High penetration of DG without any power filter increases the percentage of undesirable harmonics provided by the grid, but combined use of an inverter and active power filter allows the DG system interconnection to improve the grid tie-line flow by lowering total harmonic distortion and increasing the power factor to unity.

Keywords: Active power filter (APF); Distributed generation (DG); Solid oxide fuel cell; Inverter; Dynamic modeling; Power quality

1. Introduction

The U.S. Department of Energy (DOE) projects that total US electricity demand will increase to 5220 billion kWh in 2025 from 3481 billion kWh in 2003 [1]. There are numerous economic and societal incentives for increasing the grid capacity to meet this growth without major changes to the existing transmission infrastructure [2,3]. Adding distributed generation (DG) is a viable way to increase grid capacity while providing additional benefits over traditional electricity generation and transmission [2].

Distributed generation, which is the process of generating electricity at or near the point of its use, can both reduce the demand for transmission/generation and provide backup power [3]. Benefits of keeping generation and load physically close include high power quality, reduced transmission losses, reduced dependence on the transmission system, and improved efficiency through combined heat and power systems. Furthermore, DG provided by fuel cells could have lower environmental impact and higher electrical efficiency compared to traditional large power plants [4,5].

One of the first economically viable applications for fuel cell DG is supplying the electrical load for commercial and industrial applications that value reliable and high quality power [4,5]. Before distributed generation can be widely embraced as a future power technology, it must be demonstrated as beneficial to both the user and the connected power system. Several previous research efforts have shown control and load-following ability of DG systems [3,6,7]. This paper evaluates a sample DG-grid interconnection on the basis of experimentally measured steady-state and dynamic commercial building load data. The performance of both the DG and the grid is evaluated by investigating the effects of real building load demand on the grid tie-line current at the point of common coupling (PCC).

The individual components of the model are first described in Section 2. The methodology for load data experiment is described along with the relevant results. The DG components are a set of dynamic models created within Matlab/Simulink® that are designed to account for the physical features of a solid

* Corresponding author. Tel.: +1 949 824 1999.
E-mail address: jb@nfcrc.uci.edu (J. Brouwer).

0378-7753/$ – see front matter © 2008 Elsevier B.V. All rights reserved.
doi:10.1016/j.jpowsour.2007.12.072

oxide fuel cell (SOFC), One-Cycle Control (OCC)-based grid-connected inverter (GCI), and active power filter (APF). In Section 3, the response of each of these models is shown and compared to previous experimental results. Because directly investigating the relationship between the SOFC and the grid obfuscates the role of the inverter, Section 4 describes the inverter-grid relationship directly under steady-state conditions both with and without an active power filter. After steady-state operation is explored, the dynamic SOFC model and dynamic load data are added to the model in Section 5 to investigate grid impacts under different conditions.

2. Development of load data and models of SOFC, OCC–GCI, and OCC–APF

2.1. Load data

Data from a typical commercial Southern California office building is acquired to provide insight into the steady-state and transient power demand conditions that distributed generation might be required to meet. The 3-phase power entering the building is monitored with a Nexus model 1270 power quality monitor, which can measure both the voltage and current waveforms with user-defined sampling rates.

In order to capture detailed load transient data two sampling rates are employed. Low-frequency sampling was used to capture long-term data, while high frequency sampling was used only to capture the worst-case load transient. Both the daily power data and the worst-case transient dynamic data are presented in Fig. 1. There are two levels of power consumption: in-use during the workday and non-use at night and weekends. As seen in the close-up of Fig. 1, the power demand does not instantly jump from night load to day load, but is composed of a series of load increases as each of the several air conditioning motors turn on. The measured transient sample is the first and largest of these start-up transient building demand curves, when the building air conditioning system first turns on for the day. The 3-phase current and voltage waveforms during this start-up are sampled at 128 samples/cycle, or 7680 Hz, and the resulting instantaneous power calculation is shown in Fig. 2.

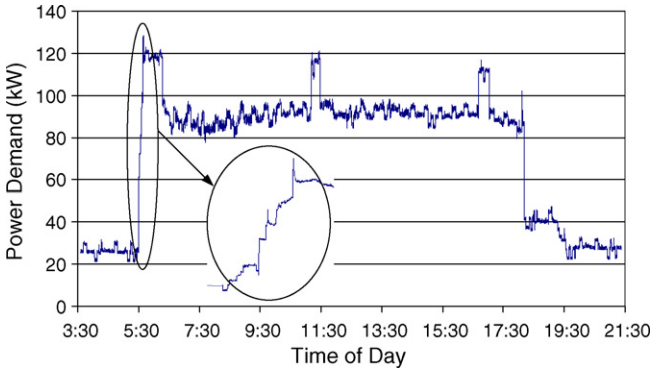

Fig. 1. Diurnal power demand for 5/24/06 with 5 s sampling interval including close-up of early AM transient with 2 s sampling interval.

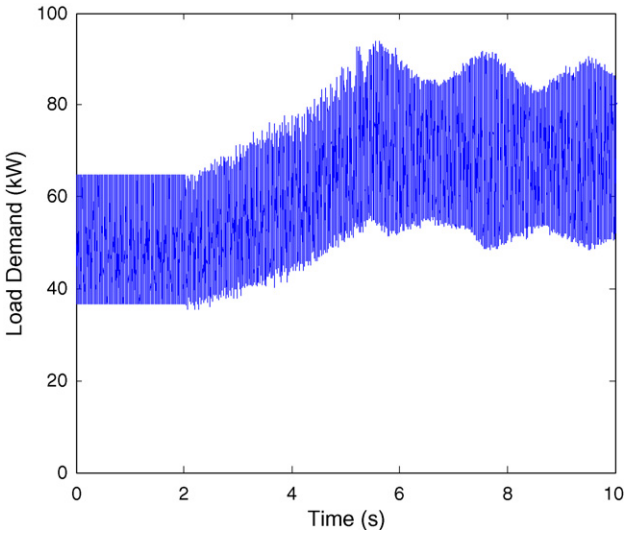

Fig. 2. Dynamic load data measured during early AM transient and sampled at 7680 Hz.

The instantaneous power exhibits a high frequency oscillation because the three fundamental phases of current average out to a constant value, but the harmonics do not.

2.2. Solid oxide fuel cell

The fuel cell type assessed in this work is a solid oxide fuel cell. SOFC technology is being rapidly advanced through significant public and private investment [8–10]. The SOFC model presented here is developed in Matlab/Simulink® according to the same methodology from [11–14], but simplified for integration with power electronics. This same methodology was used to develop models that compared favorably to experimental testing of dynamic single cell transients [15], integrated simple cycle SOFC systems [11], SOFC–MTG hybrid systems [13], and PEM stationary fuel cell systems [16].

The SOFC response is fundamentally limited by the performance of the fuel preprocessor and the amount of hydrogen present in the anode compartment [7,11,17]. The SOFC system model presented herein is therefore simplified by only capturing fuel transient effects within the fuel processor and fuel cell, which limits SOFC system transient performance. The key equations that capture fuel cell electrochemistry, hydrogen transients, and controls that are used in the present model are stated below. The fuel cell voltage shown in (1)–(5) is a common representation found in [18]. The cell voltage is the Nernst potential (E_{Nernst}) minus the activation (E_{Act}), ohmic (E_{Ohmic}), and concentration (E_{Conc}) polarizations.

$$V_{\text{cell}} = E_{\text{Nernst}} - E_{\text{Act}} - E_{\text{Ohmic}} - E_{\text{Conc}} \tag{1}$$

$$E_{\text{Nernst}} = E_0 + \frac{RT}{nF} \ln \left[\frac{X_{\text{H}_2} X_{\text{O}_2}{}^{1/2}}{X_{\text{H}_2\text{O}}} P^{1/2} \right] \tag{2}$$

$$E_{\text{Act}} = \frac{RT}{nF} \ln \left(\frac{i/A}{i_0} \right) \tag{3}$$

$$E_{\text{Ohmic}} = iR_{\text{esr}} \tag{4}$$

$$E_{\text{Conc}} = -\frac{RT}{nF}\ln\left(1 - \frac{i/A}{i_l}\right) \quad (5)$$

Hydrogen transients within the fuel cell are captured with the dynamic species conservation equation for hydrogen as in (6).

$$N\frac{dX_{H_2}}{dt} = \dot{N}_{\text{in}} - \dot{N}_{\text{out}}X_{H_2} - \dot{N}_{\text{consumed}} \quad (6)$$

The amount of reacted hydrogen is proportional to current by Faraday's law as in (7).

$$\dot{N}_{\text{consumed}} = \frac{i}{nF} \quad (7)$$

During transients it is essential that sufficient hydrogen be maintained in the fuel cell to sustain the fuel cell voltage and avoid damage caused by hydrogen starvation. Hydrogen is sustained in the anode compartment by controlling the fuel flow rate in proportion to consumed hydrogen and a desired utilization. Utilization is the amount of hydrogen consumed compared to the total hydrogen flow rate as follows:

$$U = \frac{\dot{N}_{\text{consumed}}}{\dot{N}_{\text{in}}} \quad (8)$$

From (7) the hydrogen consumption is known from the current. Therefore the required flow rate to maintain utilization can be calculated directly as in (9).

$$\dot{N}_{\text{in}} = \frac{i}{UnF} \quad (9)$$

This control strategy is called current-based fuel control and is discussed in detail in [11]. To avoid hydrogen starvation during flow delay, as explained below, i is evaluated from a look-up table that approximates the current demand from the power demand.

While power demand can change instantaneously, there is a finite time delay for fuel flow to increase. During severe transients, this delay could cause hydrogen starvation if the current drawn exceeds the available hydrogen. Limiting the fuel cell current can thus prevent hydrogen starvation. The maximum allowable current, $i_{\max}$, is defined as the current that generates a set maximum utilization, $U_{\max}$, for a given inlet hydrogen flow rate, as shown in (10).

$$i_{\max} = \dot{N}_{\text{in,delayed}}U_{\max}nF \quad (10)$$

The flow of hydrogen to the fuel cell cannot increase instantaneously because of delays in fuel delivery, preparation, and processing. The overall delay can include flow delays in valve actuation and fuel desulfurization, delays caused by the reformer chemical kinetics including those from insufficient heat transfer to the reformer and insufficient reformer residence time, as well as mass flow delays due to flow restrictions in the fuel processing system. A reformer reactor with sufficient heat transfer and residence time is assumed. Flow delays associated with the actuators, the desulfurizer, and the entire fuel processing system are lumped into a single fuel processor flow delay. The value of the fuel flow actuation delay for a fuel cell system depends upon the fuel processor design and control. Results from [7,19–22] indicate fuel processor delay times are generally on the order of seconds. Thus, the current analyses first use a hydrogen delivery delay of 2 s and include a sensitivity analysis to demonstrate the effects of fuel delay on the response and transient capability of SOFC systems.

2.3. OCC inverter

The inverter model, which is originally developed in [23] and modeled in [24], has a standard 3-phase half-bridge power stage with an OCC-based controller [25]. Six switches, S_{ap}, …, S_{cn} control the 3 phases, and inductors L_{a}, L_{b}, and L_{c} connect the half-bridges to the grid. V_{DC} is the voltage at the input DC bus, and currents i_{a}, i_{b}, and i_{c} are injected onto the grid. The circuit is constructed in Matlab/Simulink in [24] with the switching flow-graph method originally devised in [26]. The circuit and large-signal model of the power stage are shown in Fig. 3.

The grid voltage and current is sensed and processed by the OCC controller. The complete 360° 3-phase voltage window can be divided into 60° regions, during each of which the duty ratio of only two switches is actively controlled [23]. The OCC controller uses grid voltage input to select the two active switches and calculates the associated duty ratios d_{p} and d_{n} based on the

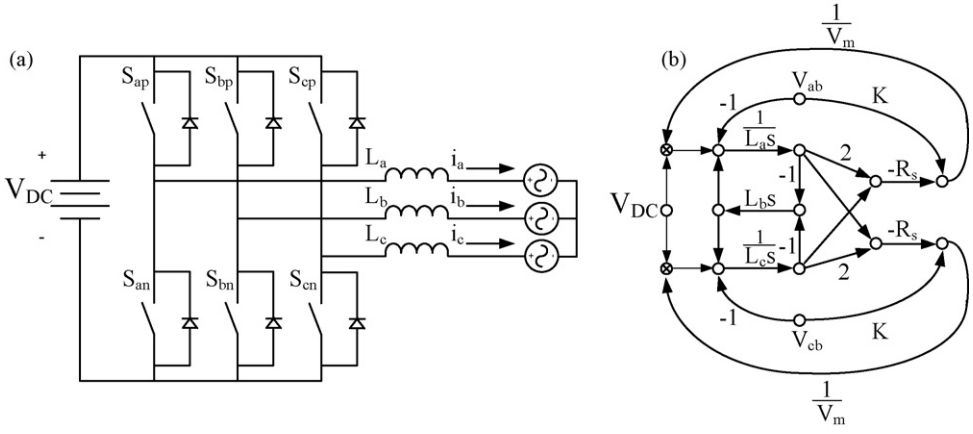

Fig. 3. Power stage circuit diagram of OCC inverter (a) and large-signal switching flow-graph model of OCC inverter (b) [24].

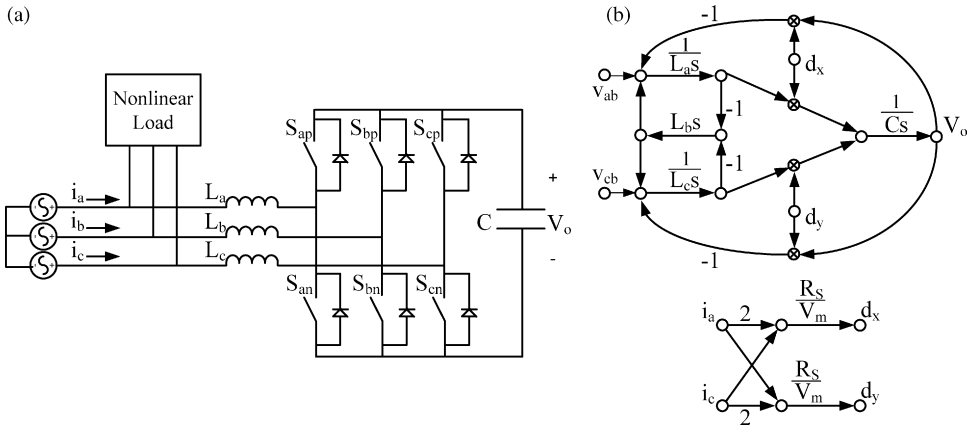

Fig. 4. Power stage circuit diagram of OCC–APF (a) and large-signal switching flow-graph model of OCC inverter (b) [31].

key control equation in (11) [23].

$$R_S \begin{bmatrix} 2 & 1 \\ 1 & 2 \end{bmatrix} \begin{bmatrix} i_p \\ i_n \end{bmatrix} = \begin{bmatrix} KV_p & -V_m d_p \\ KV_n & -V_m d_n \end{bmatrix} \tag{11}$$

R_s is the equivalent sensing resistance, K is a near-constant that limits output current, V_m is an introduced variable to control output power, i_p and i_n are selected injection currents, and V_p and V_n are selected linear combinations of grid voltages V_a, V_b, and V_c. The key control equations for K and V_m are originally derived in [24] and further developed in [27].

$$K = 1.1 R_S \left(\frac{P_{ref}}{3V_{a,rms}^2} \right) \tag{12}$$

$$V_m = \left(K - R_S \frac{P_{ref}}{3V_{a,rms}^2} \right) V_{DC} \tag{13}$$

P_{ref} is the desired output power and $V_{a,rms}$ is the rms of input grid voltage V_a.

2.4. Active power filter

The shunt active power filter (APF) compensates current harmonics from a non-linear load, balances uneven phases, and improves the power factor to one [28–30]. The OCC–APF model is originally derived in [31] by the same control and modeling technique as the inverter. The APF power stage also has 6 switches $S_{ap}, \ldots, S_{cn}$ that are configured in a 3-phase half-bridge circuit. V_o is the voltage across the capacitor C, and L_a, L_b, and L_c connect the three branches to the grid. V_a, V_b, and V_c are the grid voltages at the point of contact, and i_a, i_b, and i_c are the incoming grid currents. The power stage circuit and large-signal model are shown in Fig. 4.

Each of the six 60° regions only has two active switch pairs, and the signals to each pair are complementary. The OCC controller uses the input voltages to select which switches are active and generates the duty ratios d_p and d_n by the key control equation (14) in [28].

$$V_m \begin{bmatrix} 1 - d_p \\ 1 - d_n \end{bmatrix} = R_S \begin{bmatrix} 2 & 1 \\ 1 & 2 \end{bmatrix} \begin{bmatrix} i_p \\ i_n \end{bmatrix} \tag{14}$$

R_s is the sensing resistance, V_m is a compensated feedback of the voltage control loop, and i_p and i_n are selected input currents.

3. Verification of component models

Before they are integrated into a DG system model, the behavior of each of the previously described physical models is shown to illustrate their individual behavior. The inverter and APF models have both been previously built and tested experimentally. The component model results shown here match the experimental results. Fig. 5 shows the response of the inverter to a step change in power. The dynamic rapidly adjusts to the power increase at 5 s, and the current is sinusoidal and in step with the voltage throughout. Thus the inverter produces 3-phase current at unity power factor and low harmonic distortion, which is shown by experiments in [23,24].

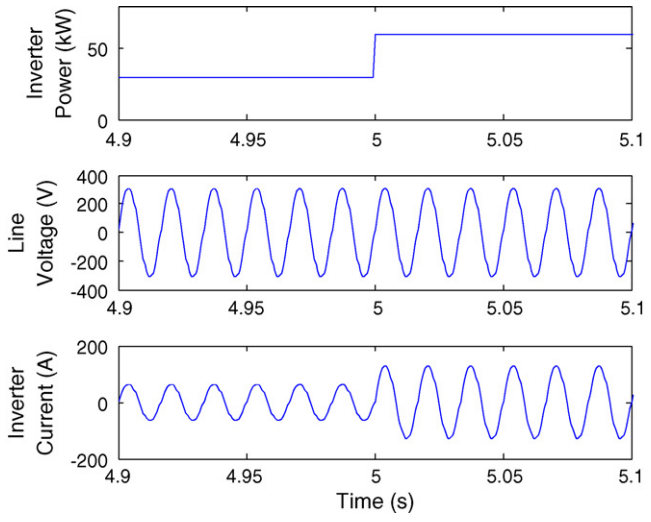

Fig. 5. Response of inverter to step power change: (top to bottom) power to inverter, phase A voltage, phase A current.

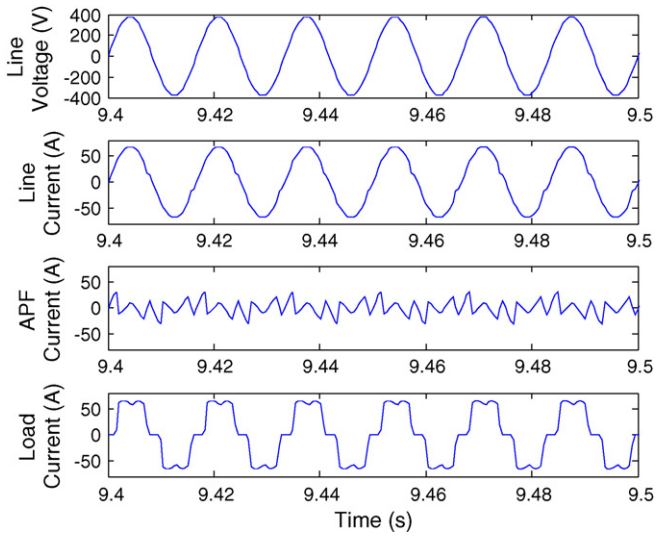

Fig. 6. Response of shunt APF to a non-linear load for phase A: (top to bottom) line voltage, compensated line current, APF compensation currents, and load current.

Simulation results for the APF model are shown in Fig. 6. A non-linear load is simulated to match the experimental load from [32]. The load current for phase A is shown at the bottom of Fig. 6, and the line voltage for phase A is shown at the top. The second graph shows the phase A grid line current after compensation, and the third graph shows the phase A compensation current from the shunt APF. All simulation results match with the experiment from [32].

The SOFC model response is presented in Fig. 7. When the power demand increases at 5 s, the SOFC stack does not have enough fuel to meet the new demand. The utilization increases to its maximum value of 90%, which allows for a slight increase in output power, but the SOFC cannot match the power demand until 7 s when the higher fuel rate can be delivered to the anode compartment. This is a direct result of the 2 s fuel flow delay in the model.

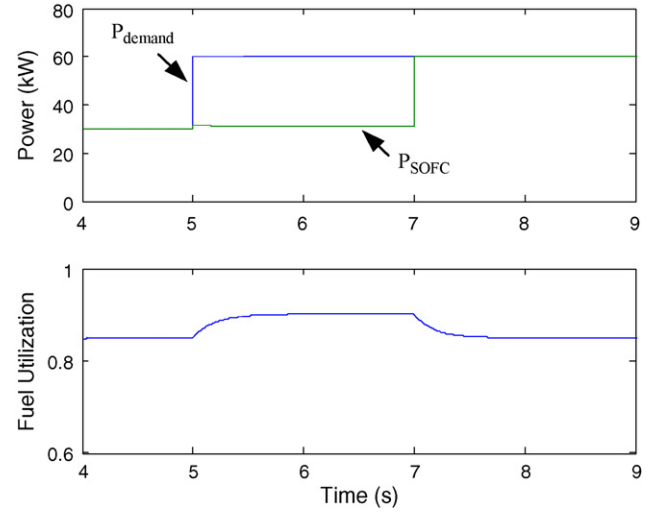

Fig. 7. Response of SOFC model to step load demand change: (top) power demand and SOFC power and (bottom) fuel utilization.

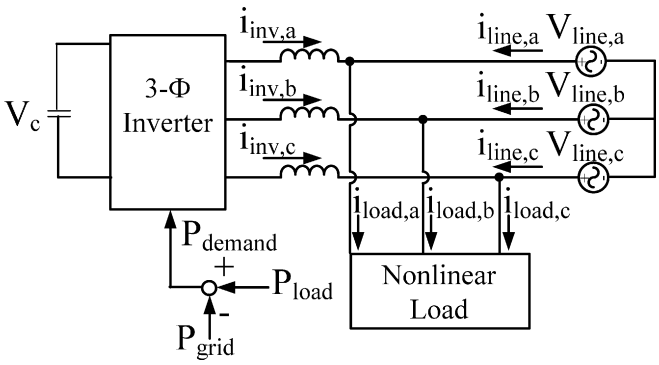

Fig. 8. Block diagram of control scheme for calculation of inverter power demand and grid connection.

4. Steady-state infinite load-following

The baseline case for the grid-connected inverter observes the grid–inverter behavior independent of the fuel cell. The power demand is measured from the load, reduced by 10 kW to avoid exportation back to the grid, and input to the inverter. To provide power in the absence of a prime mover, an infinitely large DC capacitor is assumed across the DC terminals of the inverter. The grid current is calculated instantaneously as the difference between building load current and injected inverter current. The block diagram is shown in Fig. 8 and the steady-state simulation results are shown in Fig. 9.

Tie-line current is the waveform supplied by the grid and it contains large amounts of highly undesirable distortion as shown in the bottom of Fig. 9. This distortion occurs because the inverter follows the voltage reference and is not designed to supply the higher-order harmonics that result from a non-linear load. So the inverter produces the majority of the fundamental frequency and the grid supplies the harmonics. Adding a shunt active power filter as presented in Fig. 10 eliminates this problem by providing compensation currents locally instead of from the

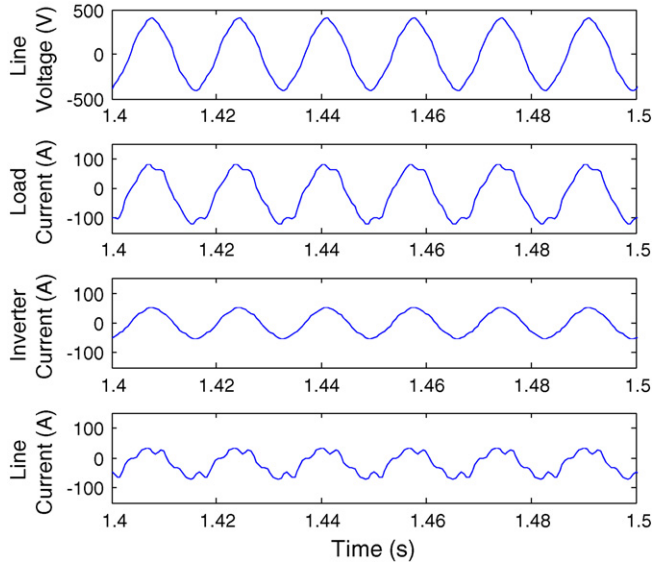

Fig. 9. Inverter-only results for phase A: (top to bottom) line voltage, load current, inverter current, and line current.

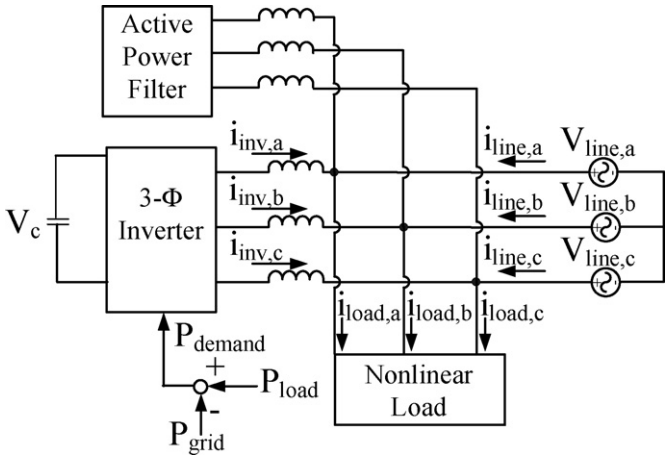

Fig. 10. Block diagram of control scheme with inverter and APF.

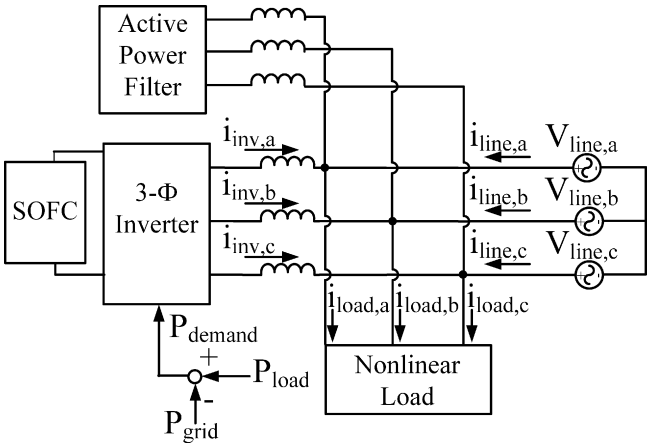

Fig. 12. Block diagram of DG system with no load-following strategy.

utility. Additional benefits of adding an APF is that it will correct the power factor of imported power to 1, and balance the phases.

The APF and inverter can be integrated into a single unit with One-Cycle Control, so adding this power quality stage would not require a substantial increase in cost or size. The line current after APF implementation is shown in Fig. 11 and shows exemplary low distortion current in the grid current.

5. Dynamic grid behavior with a solid oxide fuel cell

5.1. SOFC for load-following

Section 4 showed that a grid-beneficial scenario could be implemented through the use of an inverter and active power filter in the steady-state. The next concern is the original goal of observing grid behavior during a transient load change with a finite prime mover. The distributed energy resource used here is a SOFC that cannot immediately follow the power increase because of the delay in delivering more fuel to the fuel cell stack.

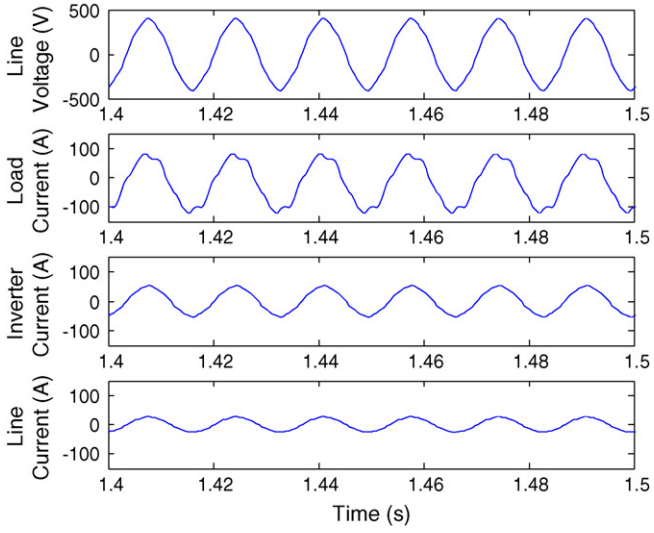

Fig. 11. Inverter with APF results for phase A: (top to bottom) line voltage, load current, inverter current, and line current.

The block diagram of the SOFC incorporation into the system is presented in Fig. 12.

The inverter calculates the power reference and low-pass filters it to protect the SOFC from the high-frequency oscillations observed in Fig. 2. The SOFC receives the power demand, and the inverter injects the available 3-phase current onto the grid. The deficiency between power delivered to the inverter and power demanded is shown at the top of Fig. 13. The power shortfall between load and SOFC is compensated by a large increase in grid tie-line current that creates a surge away from the desired grid power import. The tie-line current returns to standard levels as the SOFC power rises to match the load demand, but the existence of this spike indicates poor behavior for dynamic load-following. To alleviate this load-following problem, a DC capacitor is added to the inverter.

5.2. SOFC with capacitors for load-following

Adding a large capacitor to the DC input of the inverter augments the load-following capability. The capacitor is charged during steady-state operation and discharged during the transient

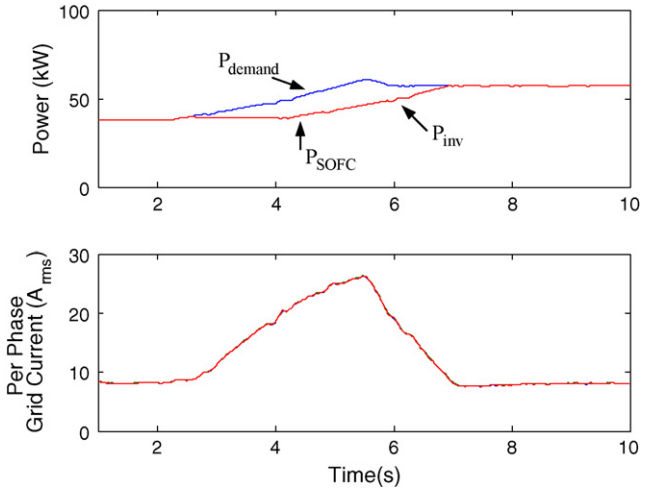

Fig. 13. SOFC with inverter and APF: (top) power demand and SOFC power and (bottom) 3-phase rms tie-line current.

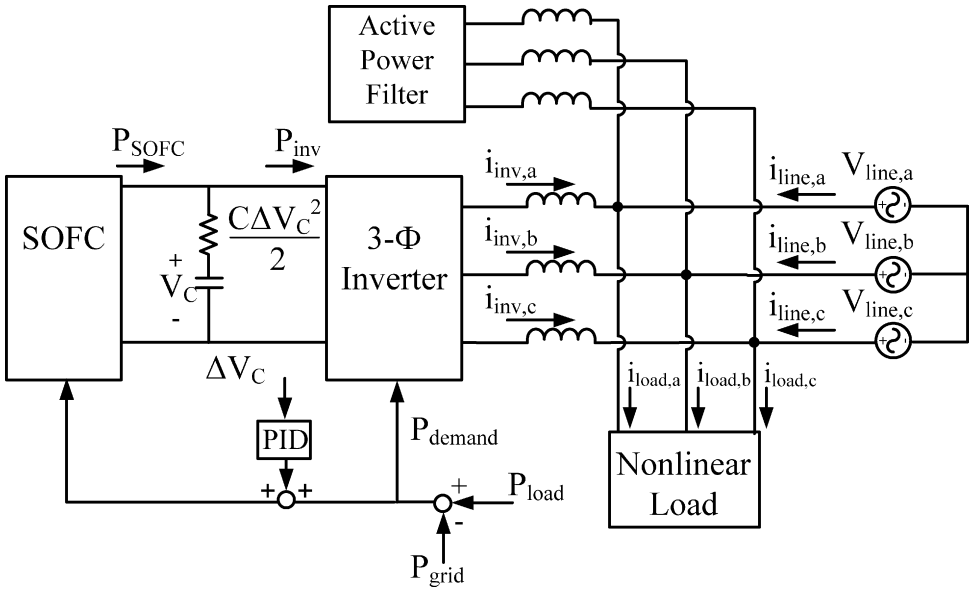

Fig. 14. Block diagram of DG system with proposed power control of DC capacitor.

power increase to supplement the SOFC power. The proposed control from [27] is used to control the voltage across a capacitor. As the capacitor voltage decreases, the difference between reference voltage and actual voltage, ΔV_c, is fed to a PID controller that increases the power demand to the fuel cell. When the fuel cell is capable of meeting the power demand, the surplus power will recharge the capacitor. The block diagram of this system is shown in Fig. 14.

The capacitance needed to completely supply the power shortfall during the transient was determined by simulating a wide range of values until the smallest value that allowed the inverter power to match the power demand was found. This value, which was 0.96 F, is designated the full capacity capacitor, and half of this value, or 0.48 F is the half capacity situation. Fig. 15 shows the full capacity scenario: the inverter power can continuously match the power demand (top), and the grid current is constant throughout the entire dynamic ramping region

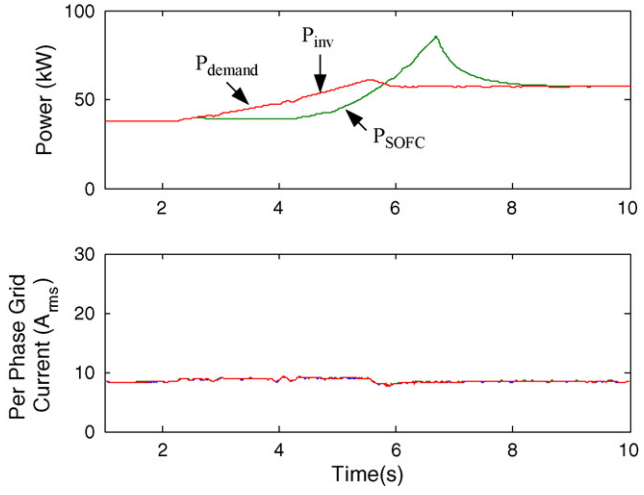

Fig. 15. SOFC with inverter, APF, and 100% DC capacitor: (top) power demand and SOFC power and (bottom) 3-phase rms tie-line current.

Table 1
Per-phase rms load current before addition of DG

Time (s)	$I_{A,rms}$	$I_{B,rms}$	$I_{C,rms}$
1.00	73.08	57.28	51.53
5.00	92.18	81.11	74.69
8.00	96.43	81.41	76.66

(bottom). The overshoot in SOFC power is the recharging of the depleted DC capacitor.

An additional result shows the value of phase balancing on the system. Table 1 shows the rms load current for each phase at selected times before, during, and after the transient. The current magnitude not only increases during the transient, but the 3 phases are clearly unbalanced. Table 2 shows the rms currents at the same times for the system that incorporates APF/Inverter DG along with a DC capacitor. The current magnitude remains constant and the phases are balanced.

Similar results for a smaller half-capacity DC capacitor are in Fig. 16. At first the inverter power can match the demand, but the capacitor voltage cannot drop too far because it is directly connected to the inverter terminals. After the capacitor is exhausted and before the SOFC can increase output, the inverter power drops and results in an increase in tie-line grid current. This current spike is less severe than for the case that is completely without capacitor storage, but it does not entirely meet the goal of a constant tie-line current.

Table 2
Per-phase rms line current with APF/inverter system

Time (s)	$I_{A,rms}$	$I_{B,rms}$	$I_{C,rms}$
1.00	8.50	8.55	8.53
5.00	8.90	8.95	8.94
8.00	8.36	8.40	8.38

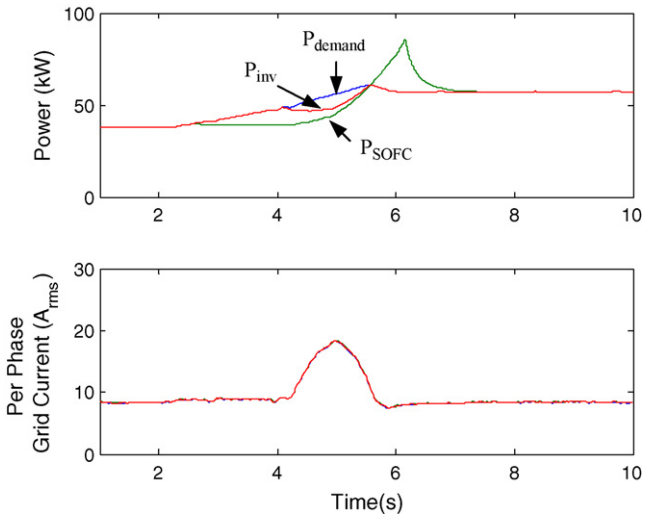

Fig. 16. SOFC with inverter, APF, and 50% DC capacitor: (top) power demand and SOFC power and (bottom) 3-phase rms tie-line current.

Table 3
Per-phase rms line current with APF/inverter system

Fuel delay (s)	DC capacitance (F)
1	0.21
2	0.96
3	1.51
4	2.07
5	2.64

The fuel flow delay is the main factor that determines the rate of response of the SOFC to a load change. As this resulting power shortfall determines the capacitor size, the estimation of fuel flow delay will correlate with the necessary capacitance as shown by a sensitivity analysis of fuel flow delay. The minimum capacitance needed for fuel delays from 1 to 5 s is shown in Table 3. The SOFC response corresponding to delays of 1 to 3 s is also shown along with the power demand in Fig. 17. The overshoot in SOFC power increases with fuel flow delay because the larger associated capacitor requires more power for recharging. In all of these cases, the charging and discharging of the DC capacitor allow the inverter power to match the load demand.

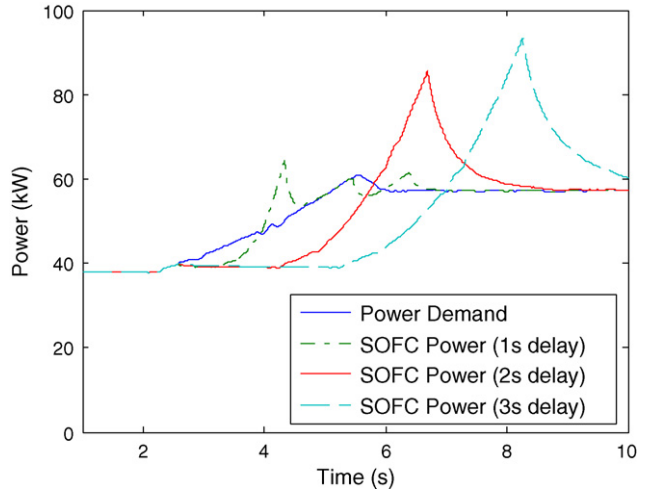

Fig. 17. Response of the SOFC power to load power demand for fuel flow delay times of 1, 2, and 3 s.

6. Conclusions

This paper has shown the development of a model designed to assess the effects of a commercial building dynamic load that incorporates DG on the electric power system at the PCC, with the goal of grid-friendly behavior. The results show that appropriate design of the DG interconnection system can provide additional benefits for the fuel cell DG and electric power system. Several physical inabilities of the fuel cell can be alleviated or eliminated with modest additions to the inverter system. Some of these inabilities addressed here include: inability for perfect load-following, inability to meet harmonics-based high frequency power demand oscillations, and inability to provide harmonics compensation. These inabilities are addressed at the inverter through the addition of an active power filter and electric energy storage.

The proposed electric energy storage strategy includes a large DC capacitor, which may be too large for actual field implementation. Thus alternative storage methods, such as ultracapacitors, batteries, and flywheels, which all have higher energy density, should be further explored. Additional concerns include a load-following ability and fuel flow delay attributed to the SOFC that may be impractical for first generation systems. One of the goals of investigating DG systems is to identify what features next generation SOFC systems will need to become successfully implemented.

The OCC-based power electronics allow a system consisting of a non-linear load and distributed generation to be seen as a simple, constant emulated resistor, even during rapid dynamic transients of prime mover and/or load.

Appendix A. Appendix

The nomenclature for the SOFC model is as follows:

A	cell surface area (m^2)
E	polarization (V)
E_0	EMF at standard pressure: 0.92 V for hydrogen and oxygen at 1000 °C
F	Faraday's constant: 96,487 C mol^{-1}
i	electrical current (A)
i_0	exchange current density (A m^{-2})
i_l	limiting current density (A m^{-2})
n	number of participating electrons in the reaction
N	molar capacity (kmol)
$\dot{N}$	molar flow rate (kmol s^{-1})
P	pressure (kPa)
R	ideal gas constant: 8.314 J K^{-1} mol^{-1}
R_{esr}	equivalent series resistance (Ω)
T	temperature (K)
U	fuel utilization
V	voltage (V)
X	species mole fraction

References

[1] United States Department of Energy, E.I.A., Annual Energy Outlook, 2005.
[2] M.K. Donnelly, et al., IEEE Trans. Power Syst. 11 (2) (1996) 741–746.
[3] C. Wang, M.H. Nehrir, H. Gao, IEEE Trans. Energy Convers. 21 (2) (2006) 586–595.
[4] R.H. Wolk, IEEE Spectrum 36 (5) (1999) 45–52.
[5] T.E. Grebe, Southcon/94 Conference Record, Orlando, FL, USA, 1994, pp. 372–377.
[6] M. Uzunoglu, M.S. Alam, IEEE Trans. Energy Conv. 21 (3) (2006) 767–775.
[7] Y. Zhu, K. Tomsovic, Electr. Power Syst. Res. 62 (2002) 1–11.
[8] M.C. Williams, J.P. Strakey, S.C. Singhal, J. Power Sources 131 (2004) 79–85.
[9] M.C. Williams, J.P. Strakey, W.A. Surdoval, J. Power Sources 143 (2005) 191–196.
[10] M.C. Williams, et al., Solid State Ionics 177 (2006) 2039–2044.
[11] F. Mueller, et al., J. Fuel Cell Sci. Technol. 3 (2006) 144–154.
[12] F. Mueller, Mechanical and Aerospace Engineering, University of California, Irvine, 2005, p. 141.
[13] R. Roberts, J. Brouwer, J. Fuel Cell Sci. Technol. 3 (2006) 18–25.
[14] F. Mueller, et al., J. Fuel Cell Sci. Technol. 3 (2007) 221–230.
[15] J. Brouwer, et al., J. Power Sources 158 (1) (2006) 213–224.
[16] K. Min, et al., Fourth International Conference on Fuel Cell Science, Technology, and Engineering, Irvine, CA, 2006.
[17] C. Haynes, J. Power Sources 109 (2) (2002) 365–376.
[18] J. Larminie, A. Dicks, Fuel Cell Systems Explained, second ed., John Wiley & Sons Ltd., 2005.
[19] T.J. Pukrushpan, G.A. Stefanopoulou, P. Huei, in: J.M. Grimble, A.M. Johnson (Eds.), Advances in Industrial Control, Springer, London, 2005.
[20] P. Beckhaus, et al., J. Power Sources 127 (2004) 249–299.
[21] F. Mueller, et al., J. Power Sources 172 (1) (2007) 308–323.
[22] F. Mueller, et al., J. Power Sources 176 (2008) 229–239.
[23] C. Qiao, K.M. Smedley, Industry Applications Conference. Thirty-sixth IAS Annual Meeting. Conference Record of the 2001 IEEE, Chicago, IL, USA, 2001, pp. 2675–2682.
[24] K. Smedley, et al., UCI and Dardel Group First International Conference on Power Electronics for Distributed and Co-generation, Irvine, CA, USA, 2004.
[25] K. Smedley, S. Cuk, IEEE Power Electronics Specialist Conference (PESC), Cambridge, MA, USA, 1991, pp. 888– 896.
[26] K. Smedley, S. Cuk, IEEE Trans. Power Electr. 9 (4) (1994) 405–413.
[27] J. Wen, K.M. Smedley, M.A. S Pai, Advanced Intelligent Mechatronics in Proceedings 2005 IEEE/ASME International Conference, Monterey, CA, USA, 2005, pp. 140–145.
[28] C. Qiao, T. Jin, K.M. Smedley, Power Electronics Specialists Conference (PESC), Vancouver, BC, Canada, 2001, pp. 1608–1614.
[29] T. Jin, C. Qiao, K.M. Smedley, IECON'01 27th Annual Conference of the IEEE Industrial Electronics Society, Denver, CO, USA, 2001, pp. 1539–1545.
[30] T. Jin, K.M. Smedley, Applied Power Electronics Conference and Exposition, Miami, FL, USA, 2003, pp. 148–153.
[31] E.M. Guiotto, K.M. Smedley, Industrial Electronics Society IECON, 2003, Roanoke, VA, USA, 2003, pp. 1067–1073.
[32] C. Qiao, T. Jin, K.M. Smedley, IEEE Trans. Ind. Electr. 51 (2) (2004) 455–463.